Improved albedo formulation for chemistry transport models based on satellite observations and assimilated snow data and its impact on tropospheric photochemistry

T. Laepple[1] and M. G. Schultz

Max Planck Institute for Meteorology, Hamburg, Germany

J. F. Lamarque, S. Madronich, R. E. Shetter, B. L. Lefer,[2] and E. Atlas[3]

Atmospheric Chemistry Division, National Center for Atmospheric Research, Boulder, Colorado, USA

[1]   Present parameterizations of the UV surface albedo in global chemistry transport models are generally based on a crude land cover classification and do not account for interannual variations of the snow-covered surface or the large variability in the albedo of snow-covered surfaces. We developed an improved scheme based on 2 years of Moderate-Resolution Imaging Spectroradiometer (MODIS) albedo data, a fine-resolution MODIS land cover map, Global Ozone Monitoring Experiment (GOME) albedo data, and daily assimilated snow cover maps from the European Centre for Medium-Range Weather Forecasts or the National Centers for Environmental Prediction. The new parameterization improves the calculation of photolysis frequencies in particular in the subarctic region as shown by a comparison of the calculated ratio of upwelling and downwelling actinic fluxes with spectral measurements from the Tropospheric Ozone Production About Spring Equinox (TOPSE) campaign (January–May 2000). The impact of surface albedo changes on tropospheric photochemistry has been investigated using the global MOZART-2 chemistry transport model. Compared with the original model version, the surface albedo changes alter the tropospheric oxidizing capacity (OH concentrations) between -20 and $+200\%$ locally and $+5\%$ in the global annual mean. About half of this change results from a new value adapted for the ocean UV albedo. Locally, NO_x concentrations were found to decrease by up to 40% and were most pronounced where the snow boundary crosses the high-emission regions in Europe, North America, and Asia. The interannual variability of snow and sea ice cover can lead to changes in the global tropospheric OH-concentration of 0.5%, which is of similar magnitude compared with the impacts of varying water vapor, transport, ozone column, and emissions as discussed in previous studies.

1. Introduction

[2]   The photochemistry in the atmosphere is largely controlled by fast reaction cycles involving radical species, such as the hydroxyl radical (OH), peroxy radicals (HO_2, RO_2), nitrate (NO_3), or halogen atoms (Br, Cl, I). Except for NO_3, which plays a significant role in nighttime chemistry, these radicals are produced through photodissociation of precursor species, and they are engaged in catalytic photochemical cycles, such as the HO_x-NO_x cycle, which governs the photochemical formation of ozone in the troposphere [*Seinfeld and Pandis*, 1998]. Accurate knowledge of the photodissociation rate coefficients is important in order to correctly simulate the budget of ozone in the troposphere, because errors translate almost linearly into errors in the net photochemical tendency of ozone [*Lefer et al.*, 2003].

[3]   The photodissociation of trace gases in the troposphere is described by

$$j = \int_{\lambda} I(\lambda)\sigma(\lambda)\Phi(\lambda)d\lambda, \tag{1}$$

---

[1]Now at Atmospheric Chemistry Division, National Center for Atmospheric Research, Boulder, Colorado, USA.

[2]Now at Department of Geosciences, University of Houston, Houston, Texas, USA.

[3]Now at Rosenstiel School of Marine and Atmospheric Sciences, University of Miami, Miami, Florida, USA.

where j denotes the photodissociation frequency, λ is wavelength, I is the actinic flux (photon density incident from all directions), σ is the absorption cross section, and ϕ is the quantum yields of different reaction pathways [*Madronich*, 1987]. The actinic flux at a given location is controlled by the incoming solar radiation (e.g., diurnal, seasonal, and solar cycles), by scattering and absorption by aerosols and clouds, by absorption by oxygen, ozone, and other gases, and by the reflection of the underlying surface, the albedo.

[4] Most photodissociation reactions require photon energies in the UV, and thus the integrand in equation (1) typically maximizes between 310 and 450 nm in the troposphere. In this study we focus on the impact of surface UV albedo changes on the actinic flux, and we discuss the impact of such changes on tropospheric ozone.

[5] On snow-free ground covered with trees, grass, or fields, the UV albedo ranges from 0.01 to 0.07 [*Schwander et al.*, 1997]. Thus reflected radiation from these surfaces has only minor impact on the photodissociation rate coefficients. Other barren surfaces (deserts) have UV albedo values up to 0.15 [*Pinker and Karnieli*, 1995]. The UV-ocean albedo of around 0.07 [*Jin et al.*, 2002] shows only a small variability. For global atmospheric chemistry modeling, a precise average value of the ocean albedo is needed because of the large area covered by water. Even though typically only about 10% of the Earth's surface is covered with snow and ice, albedo values up to 0.98 imply that the light reflected from snow- and ice-covered surfaces can have a large impact on the computed photodissociation and ozone production rates [e.g., *Beine and Krognes*, 2000].

[6] In recent years, a number of comprehensive three-dimensional models have been developed in order to simulate transport and chemistry of tropospheric ozone and its precursors. These models have been used to interpret data from field experiments and to extend the conclusions derived from these experiments by extrapolating the results to other regions and time periods [cf. *Schultz and Bey*, 2004]. The models typically include a simplified radiative transfer module (or precalculated tabulated values) to calculate the photodissociation rate coefficients taking into account the scattering and absorption from aerosols and clouds, trace gas absorption, and the surface albedo. In contrary to general circulation models, which often use complex parameterizations for the broadband surface albedo [*Roesch et al.*, 2002], current formulations of the UV albedo in numerical chemistry transport models (CTMs) typically prescribe climatological values based on a simple land cover classification [*Horowitz et al.*, 2003; *Krol and Van Weele*, 1997].

[7] However, observations show that the snow albedo shows large spatial and temporal variability and depends on several factors, such as the amount of vegetation debris falling onto the snow, masking by the canopy, or snow age or grain size. For example, *Betts and Ball* [1997] measured albedos over snow-covered boreal forest mostly lower than 0.3 while *Grenfell et al.* [1994] measured snow albedo values in Antarctica higher than 0.9. Because of the interannual variability and long-term changes in the snow extent [*Brown*, 2000; *Frei et al.*, 1999] the prescription of climatological snow cover and sea ice extent may lead to large

albedo errors over a significant fraction of the Earth's surface, and in particular near the snow line in spring.

[8] Over the last few years, various new global data products of small band surface albedo have become available from satellite instruments such as the Total Ozone mapping spectrometer (TOMS) [*Herman and Celarier*, 1997], the Global Ozone Monitoring Experiment (GOME) [*Koelemeijer et al.*, 2003], and the Moderate-Resolution Imaging Spectroradiometer (MODIS) [*Schaaf et al.*, 2002]. These data sets were derived using radiative transfer models to calculate the surface albedo from the measured top of atmosphere reflectivities taking the atmospheric effects into account. For the first time, they enable the determination of the global UV-albedo by direct measurements. In this paper we make use of these data sets to formulate a new efficient parameterization of the global UV surface albedo for use in CTM studies of specific years. Section 2 describes the methodology and the input data sets, and section 3 describes the resulting global UV albedo maps. To evaluate our approach, we use actinic flux data from aircraft measurements from the Tropospheric Ozone Production about Spring Equinox (TOPSE) campaign, which was conducted between February and May 2000 to study the evolution of tropospheric chemistry at middle to high latitudes over North America [*Atlas et al.*, 2003] (section 4). In section 5 we describe results from a global CTM simulation with the MOZART-2 chemistry transport model using our new albedo formulation and compare these to a run with the original code as described by *Horowitz et al.* [2003]. Section 6 summarizes the results and draws conclusions for further use and potential improvements.

2. Methodology

[9] The albedo of a surface is a function of wavelength as well as the angle of incidence of the radiation. For the purpose of this study we restrict ourselves to the wavelength band 280–400 nm, which is the most relevant for tropospheric photochemistry. Snow- and ice-covered surfaces, which have by far the highest UV albedos, and where accuracy is thus most important, show only a small wavelength dependence [*Grenfell et al.*, 1994]. We also neglect the variation of albedo with solar zenith angle (SZA), because the total radiation field at UV wavelengths is dominated by the diffuse sky radiation (due to Rayleigh scattering). This is especially true in snow- and ice-covered regions, where the SZA is generally large.

[10] We base our approach on two components: Monthly climatological albedo maps from the MODIS instrument on Terra [*Justice et al.*, 1998] were computed (1) for snow and (2) for nonsnow surfaces. A simple time interpolation and spatial interpolation based on the land cover type are used in order to provide global coverage for this data set, and a correction factor is applied to account for the different spectral sensitivity of the tropospheric absorbing molecules and the MODIS instrument. The albedo is then read from either the snow or the nonsnow albedo map, depending on the snow cover, which is read in daily from a numerical weather prediction model. In the following, we first describe the underlying data sets and our criteria for data selection, and then we present the composite process and validate the results by airborne actinic flux measurements. Section 2.3

Table 1. Wavelength Dependence of the Surface Albedo of Specific Land Types[a]

IGBP	Description	$\langle$Albedo (463 nm)$\rangle$/ $\langle$Albedo (380 nm)$\rangle$[b]
7	open shrublands	1.12
8	woody savannas	1.21
9	savannas	1.36
10	grasslands	1.47
12	croplands	1.18
16	barren	1.6

[a]Calculated as ratio from GOME-albedo data band 5 (463 nm) and band 2 (380 nm) [Koelemeijer et al., 2003].

[b]Band 1 (335 nm) was not used due to reported problems in this band [Koelemeijer et al., 2003]. The TOMS climatology [Herman and Celarier, 1997] suggests only a small difference of the surface albedo between 330 and 380 nm. Therefore the correction factors were directly applied on the data of MODIS band 3 (459–479 nm) to estimate the UV-surface albedo.

gives detailed information on the implementation of our albedo maps in the MOZART-2 CTM.

2.1. Available Global Albedo Data Sets

[11] From observations of the Global Ozone Monitoring Experiment (GOME) in 1995–2000, Koelemeijer et al. [2003] derived a global monthly 1° × 1° climatology of the minimum Lambert-equivalent reflectivity (MLER). These data are available for 11 wavelength bins of 1 nm width between 335 and 772 nm. However, they cannot be used directly for deriving the snow albedo maps for two reasons: (1) The GOME instrument has a rather large pixel size so that cloud contamination presents a serious problem. To reduce the effect of clouds, Koelemeijer et al. [2003] selected the minimum Lambert-equivalent reflectivity of each month. Because of the variations of the snow cover, this leads to a low bias of the snow albedo. (2) The analysis included no complex cloud correction algorithm to distinguish clouds from snow or ice.

[12] Similar problems occur with the MLER data set by Herman and Celarier [1997] derived from the Total Ozone mapping spectrometer (TOMS) in the 340- to 380-nm wavelength range. In contrast to Koelemeijer et al. [2003], their reflectivity data include a modification for partial cloud coverage whenever the reflectivity is higher than 0.08.

[13] In order to overcome these problems, we use the land surface albedo data from the visible band 3 (459–479 nm) of the MODIS instrument on Terra [Justice et al., 1998]. MODIS has a much finer resolution than GOME or TOMS and wavelength bands from the visible to the near-IR. Therefore it is better equipped to distinguish snow and ice surfaces from clouds. As the MODIS product is confined to the land surface, we assign a constant seawater albedo for all ocean surfaces that are not covered by ice. Simulations with the Coupled Ocean and Atmosphere Radiative Transfer model (COART) [Jin et al., 2002] under different conditions (chlorophyll, wind speed) suggest that the variability of the ocean UV albedo is small. Therefore a constant value seems more accurate than the GOME and TOMS UV-ocean albedo maps, which are likely to overestimate the spatial and temporal variability. The Sun zenith angle dependence of the seawater albedo was neglected in the present study.

[14] Because the MODIS instrument does not measure the UV radiation directly, we must account for the wave-length dependence of surface albedo values in different ecosystems (Table 1). The spectral dependence of the albedo for snow- and ice-covered surfaces is probably smaller than 5% between 300 and 480 nm, as suggested by in situ measurements of snow in Antarctica [Grenfell et al., 1994] as well as various other measurements of the spectral albedo [e.g., Feister and Grewe, 1995]. According to Koelemeijer et al. [2003], the wavelength dependence in woodlands and forests that are not covered by snow is smaller than 0.02. Corrections have to be made mostly in subtropical regions due to the higher wavelength dependence of grasslands and deserts (Table 1).

[15] The MODIS BDRF/Albedo product makes use of a semiempirical bidirectional reflectance (BDRF) model, and multidate cloud-free atmospheric-corrected surface reflectance observations, to provide global products of directional hemispherical albedo (so-called "black-sky albedo," i.e., direct Sun incidence neglecting incident diffuse radiation), bihemispherical albedo ("white-sky albedo," i.e., diffuse incidence only, no direct Sun), and model parameters describing the BDRF [Schaaf et al., 2002].

[16] Because of the high spatial resolution of the instrument of 500-m and wavelength bands from the visible to the near-IR, clouds and snow-covered surfaces can be detected rather well and distinguished from each other with reasonable accuracy. We used the MODIS43C1 product, which provides a 16-day composite of the land albedo on a 0.25° grid as well as quality flags and the snow coverage percentage for each pixel.

[17] As starting values for our albedo maps, we used a linear combination of 20% black sky and 80% white sky albedo of the MODIS band 3 (459–479 nm) data. This corresponds roughly to the contributions of direct and diffuse radiation to the total spectral actinic flux at 350 nm, for 60° SZA under clear-sky conditions (calculated with the tropospheric UV radiation model TUV [Madronich, 1987]). The overall results are rather insensitive to the weighting of black sky and white sky albedo: the Maximum difference is 5% in snow-covered regions. The absolute albedo difference in snow-free areas is smaller than 0.05, which corresponds to an actinic flux change of less than 10%.

[18] The quality flags of the MODIS product indicate that for creating the snow-free (snow-covered) albedo map, only 45% (25%) of the 0.25° cells were derived by the MODIS full-inversion algorithm. The other cells were derived by the MODIS backup algorithm (magnitude inversion), which is less accurate. Case studies on a snow-free region in a postlaunch validation from Jin et al. [2003a, 2003b] suggest relative accuracies of 5% for full inversion and 10% for magnitude inversion. For the purpose of this study, the lower accuracy is acceptable.

2.2. Construction of the Composite Albedo Maps

[19] In order to create monthly mean snow and snow-free albedo maps with complete global coverage, MODIS data from January 2001 to December 2002 were used. A data gap occurred in June 2001 due to instrumental problems. Each monthly 0.25° × 0.25° snow albedo map was created by averaging all the pixels that are flagged for 100% snow coverage. Missing pixels and pixels which were derived from less than four MODIS pixels were filled with snow

pixels from neighboring months. The threshold of four input pixels is a trade-off between providing seasonal variability of the albedo and producing representative data. In order to fill the remaining data gaps, we performed a multilinear regression on the observed albedo data, using the MODIS fractional land cover data [*Friedl et al.*, 2002] (International Geosphere-Biosphere Programme (IGBP) classification) as explanatory variable. Thus a yearly global average albedo value was determined for each land type. The correlation coefficient is $r^2 = 0.74$ for the snow map and $r^2 = 0.72$ for the snow-free map. The root-mean-square errors are 0.11, and 0.024, respectively. On the Antarctic plateau where no MODIS measurements exist, we adapted a value of 0.98, which is the UV-albedo of the snow cover measured by *Grenfell et al.* [1994] at the South Pole and in Vostok. We note that the likelihood of encountering snow in regions where no snow albedo data are available from MODIS is relatively small. For the analysis of the Tropospheric Ozone Production About Spring Equinox (TOPSE) experiment described below, only 1% of the albedo values were derived from interpolation. Thus deviations from the land-type correlation with the surface albedo (for example, due to orographic effects) will have only small impacts on photochemistry calculations performed with our albedo maps.

[20] A similar merging and filling by linear regression procedure was performed for snow-free pixels to get monthly snow-free albedo maps. These maps are then corrected for the wavelength dependence of the albedo in barren and sparsely vegetated surfaces and grasslands (Table 1) using the correction factors derived from the GOME albedo data set [*Koelemeijer et al.*, 2003]. The correction factors are consistent to in situ measurements by *Pinker and Karnieli* [1995]; only the correction factor for barren surfaces of 1.6 is higher than their measured wavelength dependence of $1.2-1.5$ for desert areas. The surface albedo of the wavelength corrected barren surfaces ($0.07-0.15$) agrees well with the observations.

2.3. Implementation Into the MOZART-2 CTM

[21] The MOZART-2 model [*Horowitz et al.*, 2003] is a state-of-the-art CTM for tropospheric chemistry simulations. It includes 65 species and 168 chemical reactions including 33 photodissociation reactions. In the version described by *Horowitz et al.* [2003] (hereinafter referred to as "old"), the surface albedo was parameterized according to *Müller and Brasseur* [1995]: Referring to albedo measurements at 320 nm [*Kondtratyev*, 1982], the albedo was set to 0.05 over the ocean, vegetation, and crops, 0.15 over subtropical deserts, and 0.55 over snow. The land ecosystems are taken from *Olson et al.* [1985], and a monthly sea ice climatology was taken from *Neue Welt Atlas* [1977]. Snow cover and sea ice are parameterized by the daily surface temperature. Snow over land or sea ice is assumed to cover 100% for surface temperatures below $-5°C$, with a linear variation to 0% cover for temperatures above $5°C$.

[22] In order to test our new parameterization, we use the monthly-mean satellite-derived albedo maps described above and interpolate them onto the model grid (some adjustments had to be made to values near the coastlines in order to avoid spurious averages between land and ocean albedo values). Daily assimilated data of snow cover from

National Centers for Environmental Predictin (NCEP) or European Centre for Medium-Range Weather Forecasts (ECMWF) are used to select the albedo value from the snow-covered or snow-free albedo map for each model grid box over land. Future implementations could also make use of the fractional snow cover information; however, we refrained from doing so because of the large uncertainty associated with this quantity (W. Ebisuzaki, personal communication, 2003).

[23] Over the ocean, the albedo value is set to constant values of 0.07 for the open ocean, and 0.78 and 0.89 for arctic and Antarctic sea ice, respectively. The time-dependent sea ice coverage is also taken from the NCEP or ECMWF reanalysis. The seawater albedo value represents the average value of the spectral albedo in the UV under different conditions obtained from the COART model. It is consistent with measurements at the CERES Ocean Validation Experiment (COVE) [*Jin et al.*, 2002] and with the mean value of the GOME data ocean albedo [*Koelemeijer et al.*, 2003]. On the Antarctic sea ice the surface albedo is determined almost entirely by the snow properties [*Massom et al.*, 2001]. The value we adopted is a weighted average of 90% snow albedo (0.98) and 10% first-year sea ice albedo (0.54) [*Massom et al.*, 2001; Christian Haas, personal communication, 2004]. The surface albedo on the arctic sea ice is more variable due to melting snow and pond formation [*Perovich et al.*, 2002]. Our choice of 0.78 corresponds to a UV-adjusted average value from the *Perovich et al.* [2002] data.

3. Results

[24] Figure 1 shows the (left) global snow-free and (right) snow albedo maps for the month of February (top) before and (bottom) after the interpolation and wavelength correction procedure described above. In all cases, a clear correlation with vegetation type can be observed (compare, for example, with Plate 2 of *Friedl et al.* [2002]). The interpolation procedure produces a reasonable and complete global distribution of the surface albedo in places where no snow cover (or no snow-free pixels) were observed from MODIS in 2001 and 2002. Of course, there is little practical relevance of snow albedo values in, for example, the Sahara region.

[25] The snow-free wavelength-corrected vegetation albedo generally ranges from 0.01 to 0.15 (Figure 2). Compared with the GOME UV-albedo data, most of the land types have smaller albedo values. The largest deviation occurs for the land type "evergreen broadleaf forest," where the MODIS data shows an average albedo of 0.025 whereas the corresponding land type of *Koelemeijer et al.* [2003] "tropical evergreen forest" has an average value of $0.06-0.08$. Comparing the albedo values to in situ measurement values in literature [*Doda and Green*, 1980; *Doda and Green*, 1981; *Feister and Grewe*, 1995] suggests that the GOME data overestimate the forest albedo values, perhaps due to cloud contamination. The highest snow-free albedo of up to 0.15 is observed on barren surfaces. The median value of barren surfaces of 0.10 is consistent with the "desert" value of the GOME data and with in situ measurements of *Pinker and Karnieli* [1995]. Only in small patches close to Greenland does the snow-free albedo rise up to 0.3. This is likely the effect of snow residuals in the
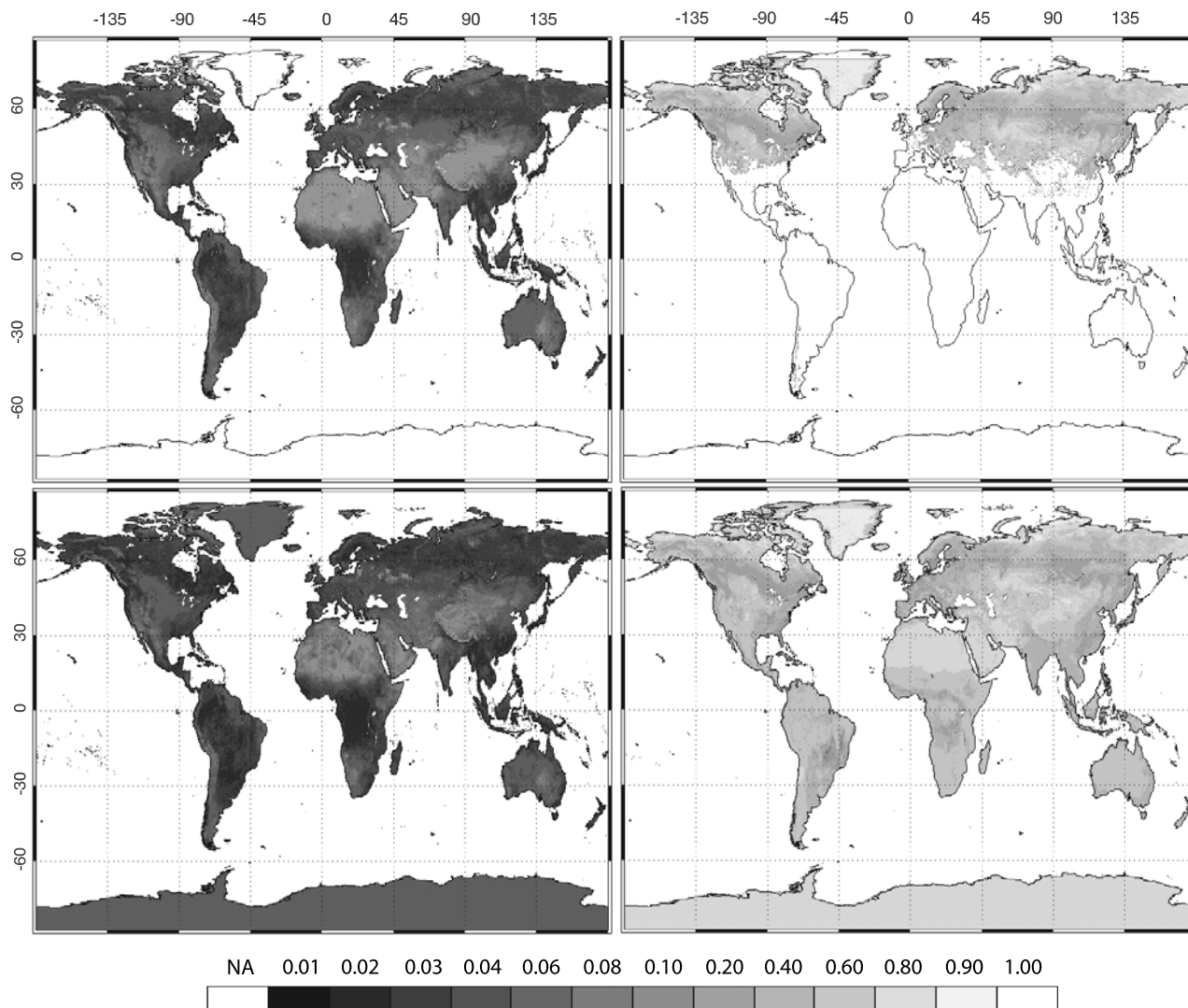
Figure 1. Albedo climatology for February derived from MODIS albedo data. (top) Before interpolation and wavelength correction. (bottom) After correction and interpolation. (left) Snow-free albedo. (right) Snow-covered albedo. For technical reasons the snow albedo values were also interpolated for desert regions. See color version of this figure at back of this issue.

16-day composite and not reliable because there are very few snow-free measurements in this area.

[26] The snow-covered vegetation albedo is mostly dependent on the density and height of the canopy. For example, the broad evergreen needle leaf forest belt in North America between 50°N and 60°N has a low snow albedo of less than 0.3. The high canopy and high coverage contribute to a large fraction of surface shadows, which results in this low albedo. These values are consistent with those reported by *Betts and Ball* [1997], considering that the latter values are broadband albedo measurements with a smaller pure snow albedo than the UV band alone. Croplands as well as grasslands south of this forest belt have higher snow albedos, around 0.6–0.7, due to smaller shadowing effects; and on barren surfaces around 60°N and 80°N, as well as on the Greenland ice sheet, the snow albedo reaches values of 0.96, which are close to the pure snow albedo in the UV [*Grenfell et al.*, 1994]. Overall, our results are consistent with the analysis by *Jin et al.* [2002].

[27] Figure 3 shows the mean albedo map for February 2001, calculated with (left) the old parameterization and (right) the new parameterization using ECMWF snow and sea ice coverage data. The albedo changes between the two parameterizations are quite substantial. There is an increase of almost a factor of 2 in many snow-covered regions (e.g., Greenland, Antarctica, and the mountainous areas in North and South America and Asia). The albedo of tropical rain forests and subtropical savannas as well as in some desert areas has been reduced, whereas a slight increase over the open ocean results from our choice of a new constant value of 0.07 instead of 0.05 used previously.

4. Evaluation of the Albedo Map Using TOPSE Data

[28] The Tropospheric Ozone production about Spring Equinox (TOPSE) experiment was conducted during February–March 2000 to study the evolution of tropospheric
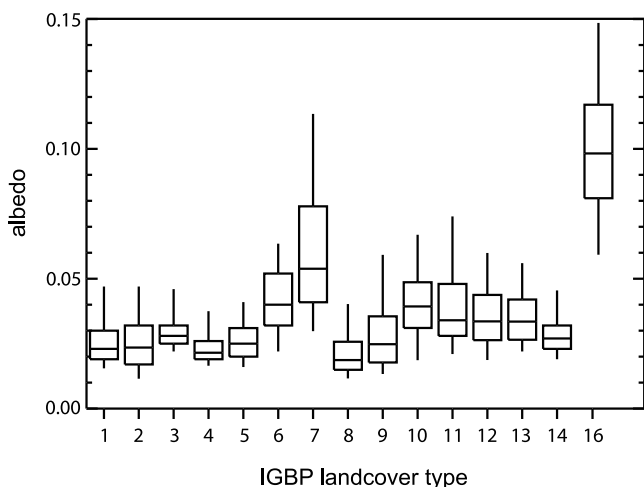
Figure 2. Median albedo values and the quartile deviation (boxes) differentiated by the IGBP land type from the snow-free albedo climatology. IGBP classification is 1, evergreen needle-leaf forests; 2, evergreen broadleaf forests; 3, deciduous needle-leaf forests; 4, deciduous broadleaf forests; 5, mixed forests; 6, closed shrublands; 7, open shrublands; 8, woody savannas; 9, savannas; 10, grasslands; 11, permanent wetlands; 12, croplands; 13, urban and built-up lands; 14, cropland/natural vegetation mosaics; 16, barren.

chemistry at middle to high latitudes over North America [*Atlas et al.*, 2003]. Spectral actinic fluxes (separately upwelling and downwelling) were measured from on board the NCAR-C130 airplane. The instrument is described by *Shetter and Muller* [1999]. The TOPSE flights covered a range of latitudes from 40°N to 87°N and encountered a variety of snow-covered vegetation as well as sea ice and snow-free regions. In order to evaluate our new global UV albedo maps, we compared the measured ratios of upwelling to downwelling actinic fluxes with model simulations with the tropospheric UV (TUV) model [*Madronich*, 1987]. This diagnostics is very sensitive to the surface albedo, with some additional contribution from Rayleigh scattering in the atmosphere below the airplane. It is independent of the absolute Sun intensity and also not very sensitive to clouds above the airplane.

[29] We used a four-stream version of the TUV code and the same wavelength range as the measurements (288–532 nm) with a spectral resolution of 1 nm. The radiative transfer model was run every minute along the aircraft flight path, using 60-s averages of latitude, longitude, temperature, altitude, and air density from the aircraft data files. Other input parameters were the ground altitude derived from the global topographic 30 arc sec map GTOPO30 (LPDAAC, 2003, available at http://edcdaac.usgs.gov/gtopo30/), the total overhead ozone column from TOMS interpolated to the airplane position, and the surface albedo value from the respective pixel in the snow or snow-free albedo map. For vertical profiles of pressure, temperature, and aerosol, the TUV standard profiles were used (U.S. Standard Atmosphere, 1967; *Elterman* [1968]).

[30] The TUV calculations and the measured flux data were averaged over 10-min intervals, and the available periods were compared. Periods where the actinic flux values were below the measurement limit of the instruments, as well as periods with a pitch or roll angle over 5°, were ignored. The results were integrated over five wavelength bins between 288 and 532 nm.

[31] All flights were taken into account regardless of the cloud cover, and the data were compared with clear-sky TUV simulations since no accurate quantitative cloud fraction data were available. For the interpretation of special
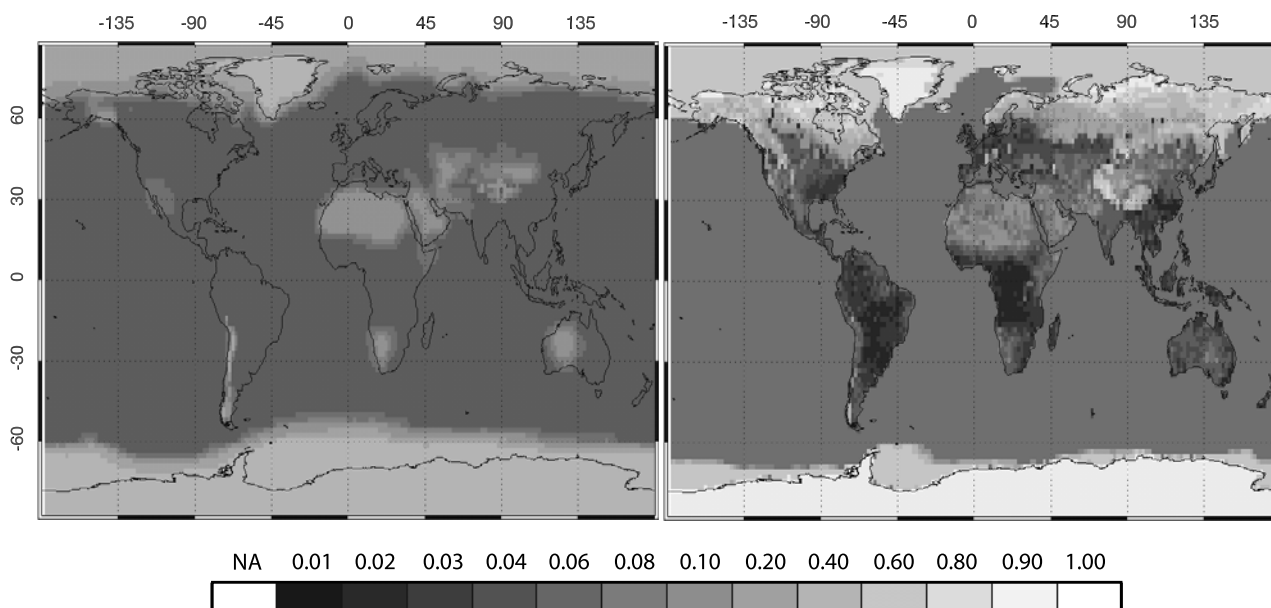
Figure 3. Monthly mean surface albedo map from the MOZART-2 model for February 2001 using the (left) old and (right) new albedo parameterization. See color version of this figure at back of this issue.
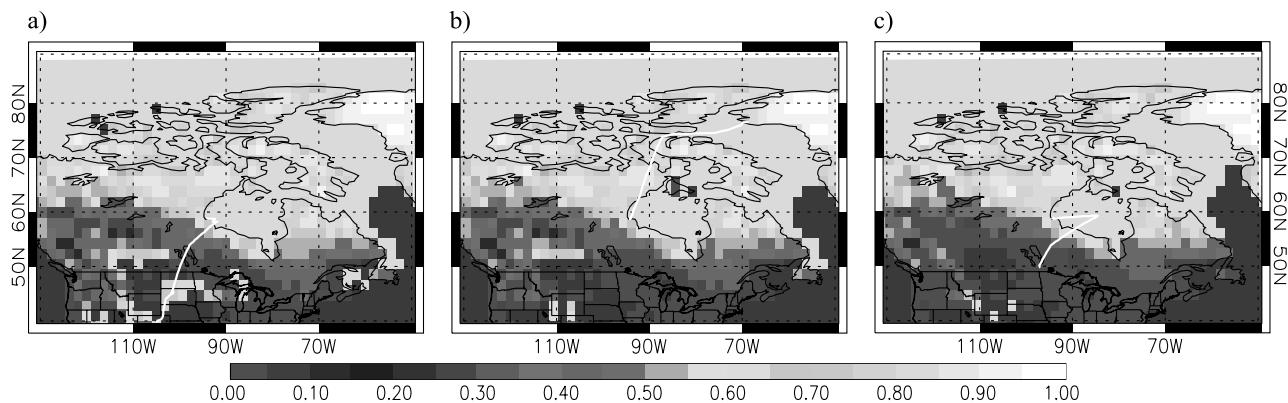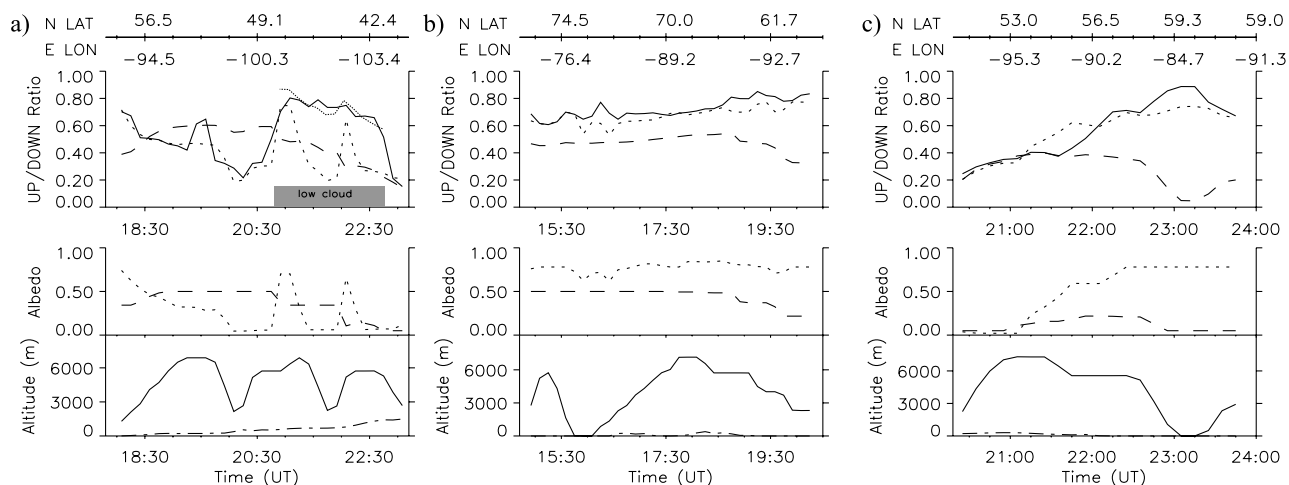
Figure 4. Albedo maps and flight tracks for (a) TOPSE flight 17 (8 March 2000), (b) flight 22 (24 March 2000), and (c) flight 32 (23 April 2000). See color version of this figure at back of this issue.

flights, qualitative cloud data derived from the lidar measurements [*Ridley et al.*, 2003] were used.

[32] Figure 4 shows the flight tracks of three selected flights superimposed on the albedo map derived from MODIS data and the NCEP reanalysis snow cover for the day of flight. The flights are mostly cloud-free below the airplane and cover different time periods and different geographic regions. Figures 5a–5c show the comparison between the measured flux ratios (solid lines) and the modeled flux ratios using the old (long-dashed lines) and new (short-dashed lines) albedo maps for three selected flights. The upper panels show the actinic flux ratios averaged over 320–380 nm, and the lower panels show the old and new surface albedo values along the flight track and the ground and flight altitudes. At higher altitudes the upwelling part of the actinic flux is enhanced due to Raleigh scattering below the airplane. It is obvious that

the surface albedo has a large impact on the simulated actinic flux ratios and that the new albedo parameterization reproduces the observed features much better.

[33] TOPSE flight 17 went from Churchill to JeffCo on 8 March 2000 (Figure 4a, Figure 5a). The overall agreement between the measured and the modeled fluxes with the new albedo map is good. In the first half of the flight the flux ratio decreases from 0.8 to nearly 0.2. The vegetation below the airplane, which gets taller and denser with decreasing latitude, reduces the snow albedo until the flight track is finally crossing the snow line at around 1945 UT. Around 45°N (2030 UT) the airplane is crossing another snow field, which has a high albedo of 0.7 due to the low vegetation. With increasing albedo the measured ratio and the modeled ratios using the new parameterization are also increasing. Around 2130 UT the observed high actinic flux ratio was due to a dense cloud below the airplane, which was

Figure 5. Comparison between measured and calculated ratios of upwelling to downwelling actinic fluxes for (a) TOPSE flight 17 (8 March 2000), (b) flight 22 (24 March 2000), and (c) flight 32 (23 April 2000). Top row shows flux ratios: solid curve, measurement; short-dashed curve, calculated with new albedo map as input; long-dashed curve, calculated with MOZART albedo map as input. (Dotted curve over the cloud in Figure 5a shows ratio calculated with the new albedo map assuming a $\tau = 20$, 1–2 km cloud layer). Bottom row shows surface albedo values and flight altitude on the airplane position: solid curve, airplane altitude; dash-dotted curve, ground altitude.

Table 2. Mean and 1σ Standard Deviation Over All the Flights of the Ratio Between Upwelling and Downwelling Actinic Fluxes[a]

Wavelength, nm	Measurement Mean (SD)	Model With MOZART Albedo			Model With New Albedo		
		Mean (SD)	RMSE	RMSEA	Mean (SD)	RMSE	RMSEA
288–329	0.648 (0.203)	0.466 (0.087)	0.260	0.208	0.575 (0.137)	0.162	0.114
330–379	0.607 (0.219)	0.445 (0.113)	0.281	0.210	0.574 (0.154)	0.156	0.092
379–429	0.575 (0.238)	0.402 (0.119)	0.297	0.224	0.532 (0.173)	0.176	0.105
430–479	0.553 (0.248)	0.374 (0.125)	0.306	0.233	0.505 (0.191)	0.186	0.111
480–532	0.537 (0.252)	0.353 (0.131)	0.310	0.238	0.487 (0.206)	0.190	0.114

[a]The ratios measured during TOPSE, modeled using the original MOZART albedo as input and using the presented new albedo map as input, are shown on different wavelength ranges. Also, the root-mean-square error (RMSE) of the model as well as the RMSE calculated from the flight average values (RMSEA) are presented.

observed by the lidar system. If we insert a cloud layer extending from 1- to 2-km altitude with an optical thickness of 20 into the radiative transfer calculations, TUV can easily reproduce the high actinic flux ratio that was observed (dotted line in Figure 2a). Unfortunately, there are not enough detailed observations available to verify these assumptions for the cloud parameters.

[34] Flight 22, Thule to Churchill on 24 March 2000 (Figure 4b, Figure 5b), passed over barren snow-covered land and sea ice and was mainly cloud free below the airplane. After 1845 UT, no cloud information is available. On this flight the MODIS snow albedo and the fixed sea ice albedo of the new model yield good agreement with the measurements. The low bias of the modeled ratios with the old albedo suggests that the snow and ice albedo values in the old albedo maps have a strong low bias.

[35] Flight 32, Winnipeg to Churchill on 23 April 2000 (Figure 4c, Figure 5c), was again cloud-free below the airplane according to the lidar measurements. The snow line already moved more than 500 km to the north in the time since flight 17 discussed above. According to the composite albedo map the flight path crossed a snow-free area until 2100 UT. Farther north, the albedo increases gradually due to snow cover on more and more sparse vegetation. The airplane reaches the sea ice at 2230 UT. Both the observed and the modeled actinic flux ratio (using the new formulation) show the same gradual increase with time. In contrast, the TUV simulation with the old albedo maps remains constant or even decreases over the Hudson Bay area. Variations of the measured actinic flux ratio in the latter part of the flight are probably due to albedo variations, which are not captured in our parameterization, because we assign a constant albedo value for sea ice.

[36] Table 2 presents the mean values and standard deviations of the actinic flux ratio in five different wavelength intervals averaged over all 37 TOPSE flights. Additionally, the root-mean-square error (RMSE) of the modeled ratios for the 10-min intervals and the RMSE over the average flux ratio for each flight (RMSEA) are shown. As observed in the individual case studies described above, the ratios and their variability calculated with the new albedo map are much closer to the measurements than the model values which use the old map.

[37] The measured mean value and the variability are always higher than the mean and the variability of the cloud-free TUV results. This can be explained by clouds below the airplane, which enhance the effective albedo and are not taken into account in the model. For shorter wavelengths, the photon path length gets shorter so that the cloud

effect is reduced and the RMSEs are decreasing (except in the shortest wavelength interval). The RMSE increase for the shortest wavelengths in Table 2 is likely due to the increased model sensitivity to the ozone column and the greater measurement uncertainty in this spectral range [*Shetter et al.*, 2002]. The calculated RMSE of the average actinic flux ratios for each flight (RMSEA) exhibits very similar behavior and thus provides evidence that the new albedo formulation will perform well on larger scales as they are typically applied in global CTMs. In spite of cloud contamination, the average actinic flux ratios stay within 9–11% of the observations using the new albedo maps compared with 20–24% when the old albedo formulation is used.

5. Implications of the New Albedo Maps on Tropospheric Chemistry Simulations

[38] In order to study the impacts of the new albedo parameterization on the calculation of photolysis frequencies, trace gas concentrations, and the chemical rate of ozone formation and destruction, we have performed two test simulations with the MOZART-2 CTM [*Horowitz et al.*, 2003] for January–April 2001. The model was driven by operational analyses from ECMWF, and the resolution was $1.8° \times 1.8°$ longitude × latitude with 47 vertical levels from the surface to 10 hPa. Compared with the version described by *Horowitz et al.* [2003], the model version we used has been improved by implementing an interactive dry deposition scheme based on *Wesely* [1989] and by revising the parameterization of lightning NO_x production based on results obtained from comparisons with measurements obtained in the CRYSTAL-FACE experiment [*Ridley et al.*, 2004]. We performed one reference simulation with the standard albedo formulation as described by *Müller and Brasseur* [1995] (hereinafter referred to as R1), and one simulation using our new albedo maps and the daily ECMWF snow cover fields as described in section 2.3 (R2). We selected the winter/spring period of 2001 because we expect the largest impacts on the photochemistry during this time period, when large parts of the Northern Hemisphere continents are covered with snow. The model was initialized with simulation results for December from a previous simulation.

[39] The changes in the albedo map (Figure 3) lead to significant changes in the photolysis frequencies calculated in the model (Figure 6). The UV photolysis of ozone $j(O_3 \rightarrow O(^1D) + O_2)$, which is the primary source for OH radicals in the atmosphere, increases by more than a
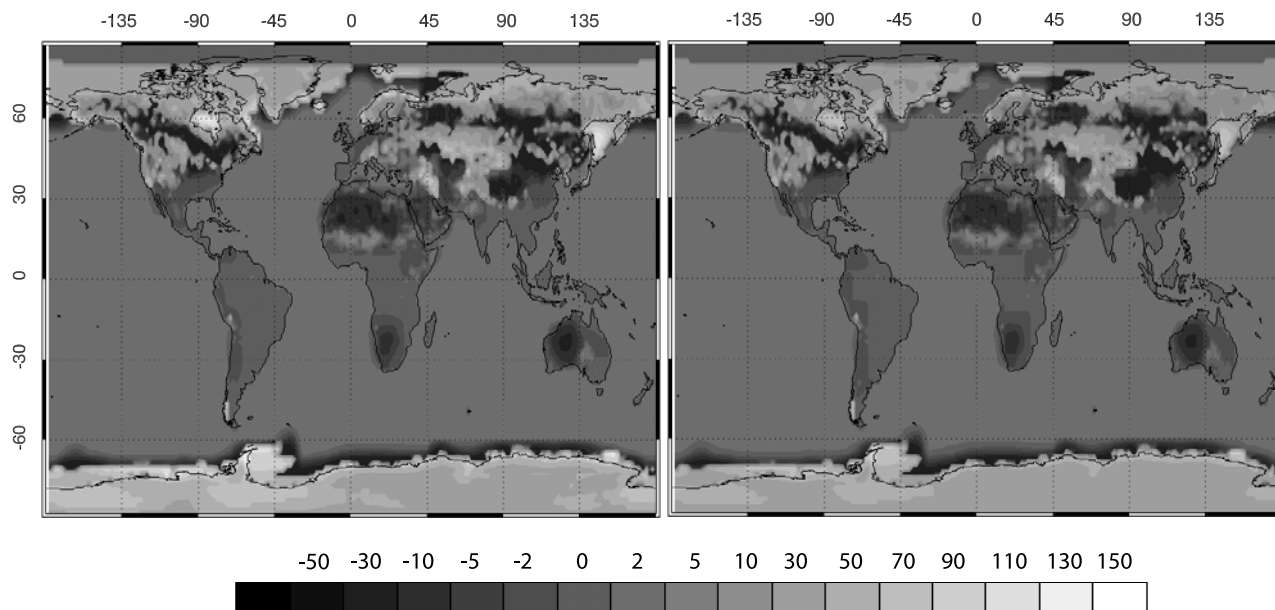
Figure 6. Relative changes (percent) of the February 2001 monthly mean value of the photolysis frequencies (left) $j(O_3 \rightarrow O(^1D) + O_2)$ and (right) $j(NO_2 \rightarrow NO + O)$. See color version of this figure at back of this issue.

factor of 2 in some snow-covered regions, in particular near the snow line. On the other hand, there is a reduction of $j(O_3 \rightarrow O(^1D) + O_2)$ of more than 20% in other areas, for example, over the Sahara. The change patterns for $j(NO_2 \rightarrow NO + O)$ look very similar; here the impact also ranges from −20% to +100%.

[40] Because of increased Rayleigh scattering at shorter wavelengths, the vertical extent of the surface albedo changes is larger for $j(NO_2 \rightarrow NO + O)$ than for $j(O_3 \rightarrow O(^1D) + O_2)$ (Figure 7). This is consistent with results from *Krol and Van Weele* [1997]. In both cases, the new albedo maps yield about 25% higher photolysis frequencies at about 5-km altitude over Antarctica, and the zonal mean

j values are enhanced by more than 10% at 5-km altitude in the Northern Hemisphere midlatitudes.

[41] These changes in the photolysis frequencies have a profound impact on the model photochemistry; in particular, they affect the fast radical cycling reactions, which ultimately control the oxidizing capacity of the atmosphere and tropospheric ozone formation. Increased $j(O_3 \rightarrow O(^1D) + O_2)$ will on the one hand lead to more efficient formation of OH radicals, which increases the oxidation rates of CO, methane, and other hydrocarbons, and thus generates more peroxy radicals (HO_2, RO_2) [cf. *Seinfeld and Pandis*, 1998]. The concurrent enhancement of $j(NO_2 \rightarrow NO + O)$ will on the other hand shift the NO/NO_2 ratio in favor of NO and
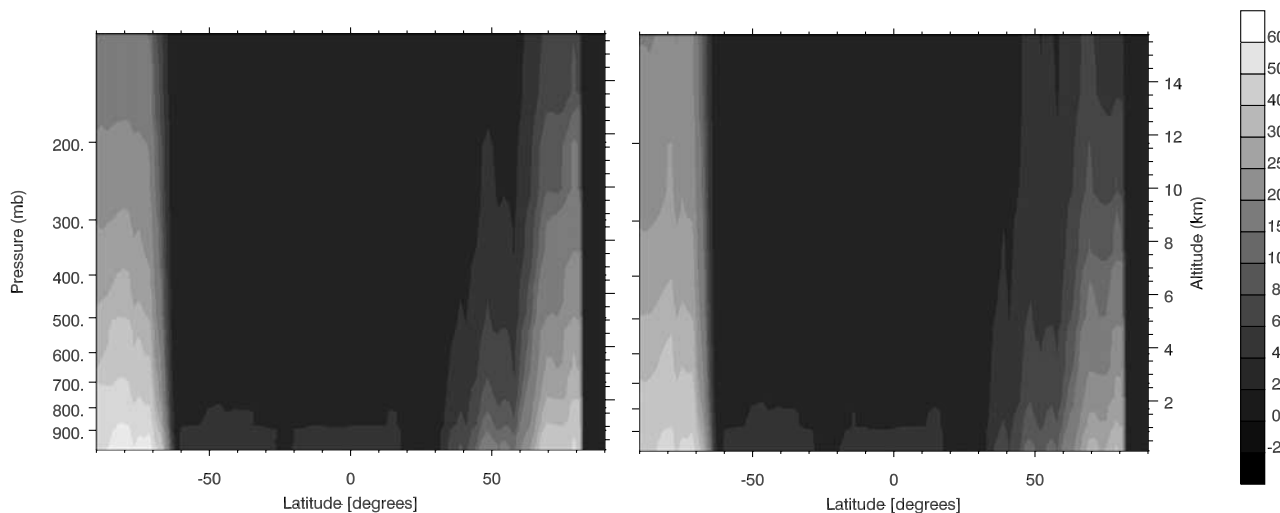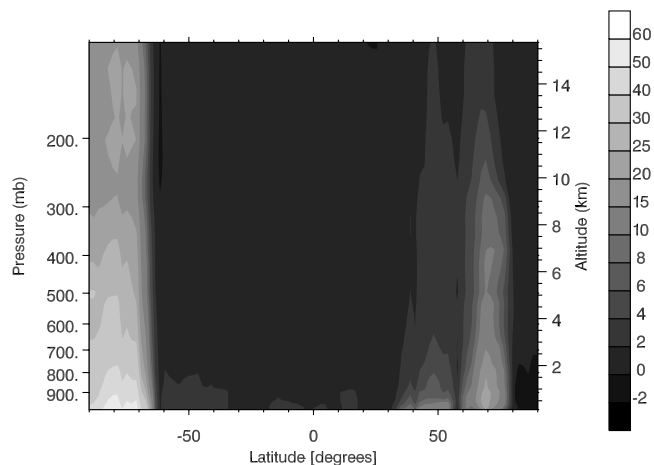

Figure 7. Zonal mean percent differences in monthly mean photolysis frequencies for February 2001: (left) $j(O_3 \rightarrow O(^1D) + O_2)$ and (right) $j(NO_2 \rightarrow NO + O)$. See color version of this figure at back of this issue.
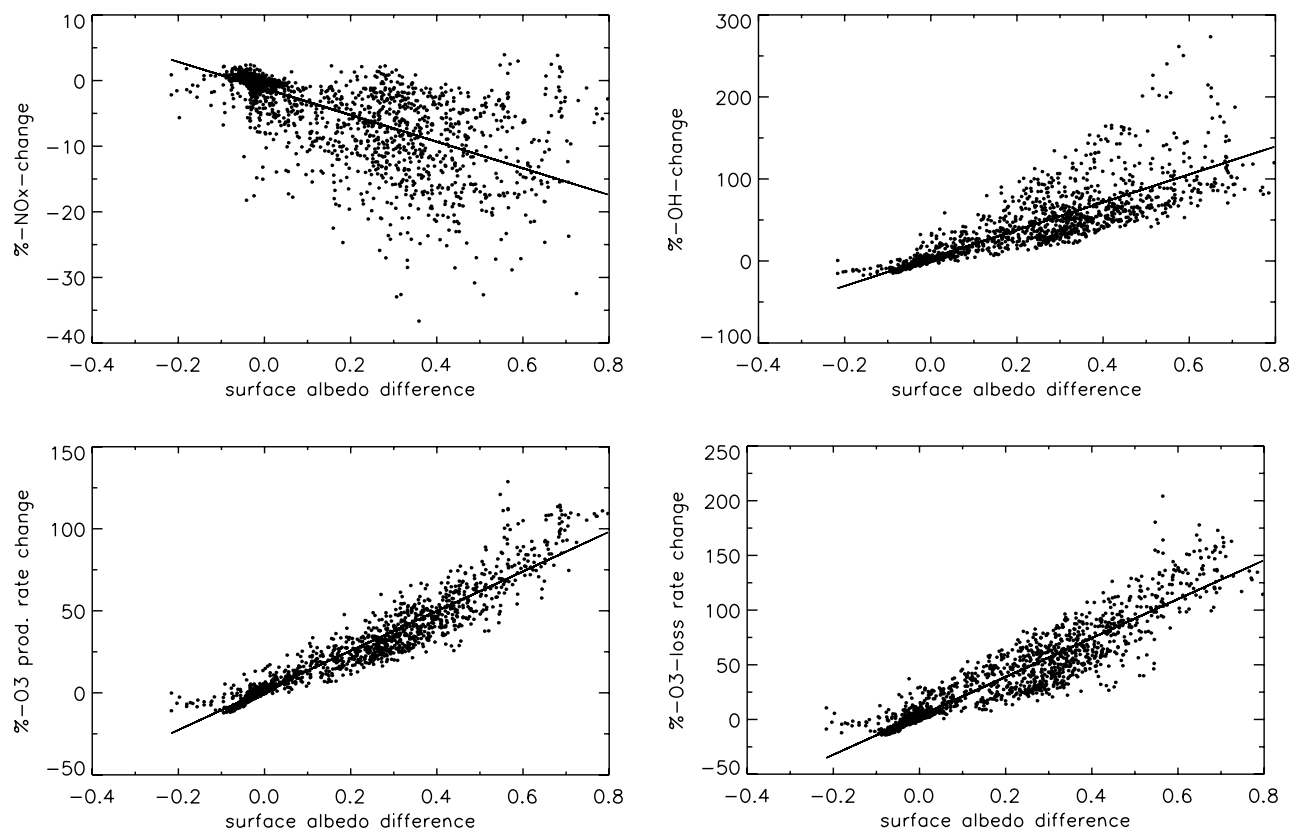
Figure 8. Simulated changes in monthly mean ground-level NO_x and OH mixing ratios for February 2001 and their dependency on the surface albedo changes from runs R1 and R2. In order to avoid spurious percent change values due to very low light intensities, only data where $j(NO_2 \rightarrow NO + O)$ are greater 2×10^{-3} s^{-1} are presented here. For clarity, we also restricted the data to continental surfaces by excluding all points with surface albedo values for sea ice and open ocean. The slopes of the linear regression lines are 20.02 for NO_x, 170.1 for OH, 120.8 for O_3 production. and 177.8 for O_3 loss. The offsets are insignificant.

thus allow more peroxy radicals to be cycled back, forming again OH. Increased OH levels also enhance the dominant NO_x loss mechanism (reaction of NO_2 with OH to form nitric acid), an effect which is somewhat dampened due to the shift in the NO/NO_2 ratio toward NO [*Krol and Van Weele*, 1997]. Figure 8 summarizes the effects of the albedo changes on ground-level mixing ratios of NO_x, OH, and ozone formation. NO_x concentrations are reduced by up to 40%, whereas OH mixing ratios increase by up to a factor of 3 between R1 and R2. A linear regression predicts a NO_x decrease of 2% and an enhancement of OH by 17% per albedo change of 0.1. Ozone production and loss rates are predicted to be enhanced by 12% and 18%, respectively.

[42] The zonal average OH concentration is especially enhanced near the snow lines, but also significant in the midlatitudes (Figure 9). An additional sensitivity run using the new albedo formulation (as in R2), but the previous ocean albedo value of 0.05 (as in R1), was performed to separate the effects of the improved snow treatment and the changed ocean albedo. The global OH concentrations are sensitive to the ocean albedo due to the high OH concentrations in the midlatitudes (65% of the global mean differences between R1 and R2 are due to the changed ocean albedo). In contrast, the global NO_x budget is more sensitive to the snow albedo changes. (Only 14% of the global mean

Figure 9. Zonal mean percent differences of OH concentration for February 2001. See color version of this figure at back of this issue.

differences between R1 and R2 are due to the changed ocean albedo.)

6. Conclusions

[43] We developed a new UV surface albedo parameterization for global CTMs by combining monthly snow and nonsnow climatologies derived from the MODIS albedo product with real-time snow and ice cover data from numerical weather prediction models. In order to evaluate this approach, we compared spectrally resolved actinic flux ratios from the new model with those measured during the TOPSE campaign in winter/spring 2000. The results show a significant improvement (average RMSE is reduced by a factor of 2) compared with the albedo formulation from the original MOZART-2 CTM as described by *Horowitz et al.* [2003].

[44] The improvements result from a better determination of the snow and ice line and from the use of a measured snow albedo climatology which takes into account the masking effect of the vegetation. A sensitivity study with the MOZART-2 CTM indicates significant changes for the tropospheric oxidizing capacity and ozone formation. For the month of February 2001, NO_x concentrations decrease locally by up to 40%, and OH concentrations increase by up to 200% due to the albedo changes. The simulations indicate that the original version of MOZART-2 underestimated the annual tropospheric OH concentration by 5%.

[45] We attempt a first estimate of the impact of interannual varying snow and sea ice cover on the global OH concentration. Multiannual observations of continental snow cover and sea ice distributions [*Brown*, 2000; *Cavalieri et al.*, 2003] exhibit an interannual variability of 20×10^5 km^2 (8%) for the snow cover, 5×10^5 km^2 (3.8%) for the arctic sea ice cover, and 7×10^5 km^2 (5%) for the Antarctic sea ice cover. These changes correspond to a variability of the snow/sea ice covered area of 3.5% (NH) and 2.5% (SH) relative to the total areas between $30°$–$80°N$ and $55°$–$75°S$, respectively. Applying the linear relationship between OH and surface albedo found in our sensitivity experiments to the averaged OH concentrations in these latitude bands, we find a potential change in the global mean OH concentration of 1% in the boundary layer and 0.5% integrated over the whole troposphere. These changes are comparable in magnitude to those found for varying water vapor, transport, ozone columns, and emissions described by *Dentener et al.* [2003], and should thus be taken into account in future modeling studies looking at the global oxidizing capacity.

[46] Because of the importance of the surface albedo in determining the magnitude and sign of climate radiative forcing from aerosols, accurate wavelength-dependent albedo parameterizations with correct treatment of snow- and ice-covered surfaces are also crucial for climate studies.

References

Atlas, E. L., B. A. Ridley, and C. A. Cantrell (2003), The Tropospheric Ozone Production about the Spring Equinox (TOPSE) Experiment: Introduction, *J. Geophys. Res.*, *108*(D4), 8353, doi:10.1029/2002JD003172.

Beine, H. J., and T. Krognes (2000), The seasonal cycle of peroxyacetyl nitrate (PAN) in the European Arctic, *Atmos. Environ.*, *34*(6), 933–940.

Betts, A. K., and J. H. Ball (1997), Albedo over the boreal forest, *J. Geophys. Res.*, *102*(D24), 28,901–28,909.

Brown, R. D. (2000), Northern Hemisphere snow cover variability and change, 1915–97, *J. Clim.*, *13*(13), 2339–2355.

Cavalieri, D. J., C. L. Parkinson, and K. Y. Vinnikov (2003), Thirty-year satellite record reveals contrasting Arctic and Antarctic decadal sea ice variability, *Geophys. Res. Lett.*, *30*(18), 1970, doi:10.1029/2003GL018031.

Dentener, F., W. Peters, M. Krol, M. van Weele, P. Bergamaschi, and J. Lelieveld (2003), Interannual variability and trend of CH_4 lifetime as a measure for OH changes in the 1979–1993 time period, *J. Geophys. Res.*, *108*(D15), 4442, doi:10.1029/2002JD002916.

Doda, D. D., and A. E. S. Green (1980), Surface reflectance measurements in the ultraviolet from an airborne platform: 1, *Appl. Opt.*, *19*(13), 2140–2145.

Doda, D. D., and A. E. S. Green (1981), Surface reflectance measurements in the ultraviolet from an airborne platform: 2, *Appl. Opt.*, *20*(4), 636–642.

Elterman, L. (1968), UV, visible, and IR attenuation for altitudes to 50 km, *Environ. Res. Pap. AFCRL NTIS-AD 671933*, 58 pp., U.S. Air Force Cambridge Res. Lab., Cambridge, Mass.

Feister, U., and R. Grewe (1995), Spectral albedo measurements in the ultraviolet and visible region over different types of surfaces, *Photochem. Photobiol.*, *62*(4), 736–744.

Frei, A., D. A. Robinson, and M. G. Hughes (1999), North American snow extent: 1900–1994, *Int. J. Climatol.*, *19*(14), 1517–1534.

Friedl, M. A., et al. (2002), Global land cover mapping from MODIS: Algorithms and early results, *Remote Sens. Environ.*, *83*(1–2), 287–302.

Grenfell, T. C., S. G. Warren, and P. C. Mullen (1994), Reflection of solar radiation by the Antarctic snow surface at ultraviolet, visible, and near-infrared wavelengths, *J. Geophys. Res.*, *99*(D9), 18,669–18,684.

Herman, J. R., and E. A. Celarier (1997), Earth surface reflectivity climatology at 340–380 nm from TOMS data, *J. Geophys. Res.*, *102*(D23), 28,003–28,011.

Horowitz, L. W., et al. (2003), A global simulation of tropospheric ozone and related tracers: Description and evaluation of MOZART, version 2, *J. Geophys. Res.*, *108*(D24), 4784, doi:10.1029/2002JD002853.

Jin, Y.-F., C. B. Schaaf, F. Gao, X. W. Li, A. H. Strahler, W. Lucht, and S.-L. Liang (2003a), Consistency of MODIS surface bidirectional reflectance distribution function and albedo retrievals: 1. Algorithm performance, *J. Geophys. Res.*, *108*(D5), 4158, doi:10.1029/2002JD002803.

Jin, Y.-F., C. B. Schaaf, C. E. Woodcock, F. Gao, X.-W. Li, A. H. Strahler, W. Lucht, and S.-L. Liang (2003b), Consistency of MODIS surface bidirectional reflectance distribution function and albedo retrievals: 2. Validation, *J. Geophys. Res.*, *108*(D5), 4159, doi:10.1029/2002JD002804.

Jin, Z. H., T. P. Charlock, and K. Rutledge (2002), Analysis of broadband solar radiation and albedo over the ocean surface at COVE, *J. Atmos. Oceanic Technol.*, *19*(10), 1585–1601.

Justice, C. O., et al. (1998), The Moderate Resolution Imaging Spectroradiometer (MODIS): Land remote sensing for global change research, *IEEE Trans. Geosci. Remote Sens.*, *36*(4), 1228–1249.

Koelemeijer, R. B. A., J. F. de Haan, and P. Stammes (2003), A database of spectral surface reflectivity in the range 335–772 nm derived from 5.5 years of GOME observations, *J. Geophys. Res.*, *108*(D2), 4070, doi:10.1029/2002JD002429.

Kondratyev, K. Y. (1982), The shortwave albedo and the surface emissivity, in *Land Surface Processes in Atmospheric Circulation Models*, edited by P. Eagleson, pp. 463–514, Cambridge Univ. Press, New York.

Krol, M. C., and M. Van Weele (1997), Implications of variations in photodissociation rates for global tropospheric chemistry, *Atmos. Environ.*, *31*(9), 1257–1273.

Lefer, B. L., R. E. Shetter, S. R. Hall, J. H. Crawford, and J. R. Olson (2003), Impact of clouds and aerosols on photolysis frequencies and photochemistry during TRACE-P: 1. Analysis using radiative transfer and photochemical box models, *J. Geophys. Res.*, *108*(D21), 8821, doi:10.1029/2002JD003171.

Madronich, S. (1987), Photodissociation in the atmosphere: 1. Actinic flux and the effects of ground reflections and clouds, *J. Geophys. Res.*, *92*(D8), 9740–9752.

Massom, R. A., et al. (2001), Snow on Antarctic sea ice, *Rev. Geophys.*, *39*(3), 413–445.

Müller, J. F., and G. Brasseur (1995), IMAGES: A three-dimensional chemical transport model of the global troposphere, *J. Geophys. Res.*, *100*(D8), 16,445–16,490.

Neue Welt Atlas (1977), Reise und Verkehrsverlag GmbH, Berlin-Götersloh-Stuttgart, Germany.

Olson, J. S., J. A. Watts, and L. J. Allison (1985), Major world ecosystems complexes ranked by carbon live vegetation, A database, in *ORNL-5862*, 164 pp., Oak Ridge Natl. Lab., Oak Ridge, Tenn.

Perovich, D. K., T. C. Grenfell, B. Light, and P. V. Hobbs (2002), Seasonal evolution of the albedo of multiyear Arctic sea ice, *J. Geophys. Res.*, *107*(C10), 8044, doi:10.1029/2000JC000438.

Pinker, R. T., and A. Karnieli (1995), Characteristic spectral reflectance of a semiarid environment, *Int. J. Remote Sens.*, *16*(7), 1341–1363.

Ridley, B. A., et al. (2003), Ozone depletion events observed in the high-latitude surface layer during the TOPSE aircraft program, *J. Geophys. Res.*, *108*(D4), 8356, doi:10.1029/2001JD001507.

Ridley, B., et al. (2004), Florida thunderstorms: A faucet of reactive nitrogen to the upper troposphere, *J. Geophys. Res.*, *109*, D17305, doi:10.1029/2004JD004769.

Roesch, A., M. Wild, R. Pinker, and A. Ohmura (2002), Comparison of spectral surface albedos and their impact on the general circulation model simulated surface climate, *J. Geophys. Res.*, *107*(D14), 4221, doi:10.1029/2001JD000809.

Schaaf, C. B., et al. (2002), First operational BRDF, albedo nadir reflectance products from MODIS, *Remote Sens. Environ.*, *83*(1–2), 135–148.

Schultz, M. G., and I. Bey (2004), Numerical modelling of long-range pollution transport, in *The Handbook of Environmental Chemistry*, pp. 198–220, Springer, New York.

Schwander, H., P. Koepke, and A. Ruggaber (1997), Uncertainties in modeled UV irradiances due to limited accuracy and availability of input data, *J. Geophys. Res.*, *102*(D8), 9419–9429.

Seinfeld, J. H., and S. N. Pandis (1998), *Atmospheric Chemistry and Physics: From Air Pollution to Climate Change*, John Wiley, Hoboken, N. J.

Shetter, R. E., and M. Muller (1999), Photolysis frequency measurements using actinic flux spectroradiometry during the PEM-Tropics mission: Instrumentation description and some results, *J. Geophys. Res.*, *104*(D5), 5647–5661.

Shetter, R. E., L. Cinquini, B. L. Lefer, S. R. Hall, and S. Madronich (2002), Comparison of airborne measured and calculated spectral actinic flux and derived photolysis frequencies during the PEM Tropics B mission, *J. Geophys. Res.*, *108*(D2), 8234, doi:10.1029/2001JD001320.

Wesely, M. L. (1989), Parameterization of surface resistances to gaseous dry deposition in regional-scale numerical models, *Atmos. Environ.*, *23*(6), 1293–1304.

———————————

E. Atlas, Rosenstiel School of Marine and Atmospheric Sciences/MAC, University of Miami, 4600 Rickenbacker Causeway, Miami, FL 33149-1098, USA.

T. Laepple, J. F. Lamarque, S. Madronich, and R. E. Shetter, Atmospheric Chemistry Division, National Center for Atmospheric Research, 1850 Table Mesa Drive, Boulder, CO 80307, USA. (laepple@dkrz.de)

B. L. Lefer, Department of Geosciences, University of Houston, 312 SRB-1, 4800 Calhoun Road, Houston, TX 77204-5007, USA.

M. G. Schultz, Aerosol, Chemistry, and Climate Group, Department of Atmosphere in the Earth System, Max-Planck-Institut für Meteorologie, Bundesstrasse 55, D-20146 Hamburg, Germany.
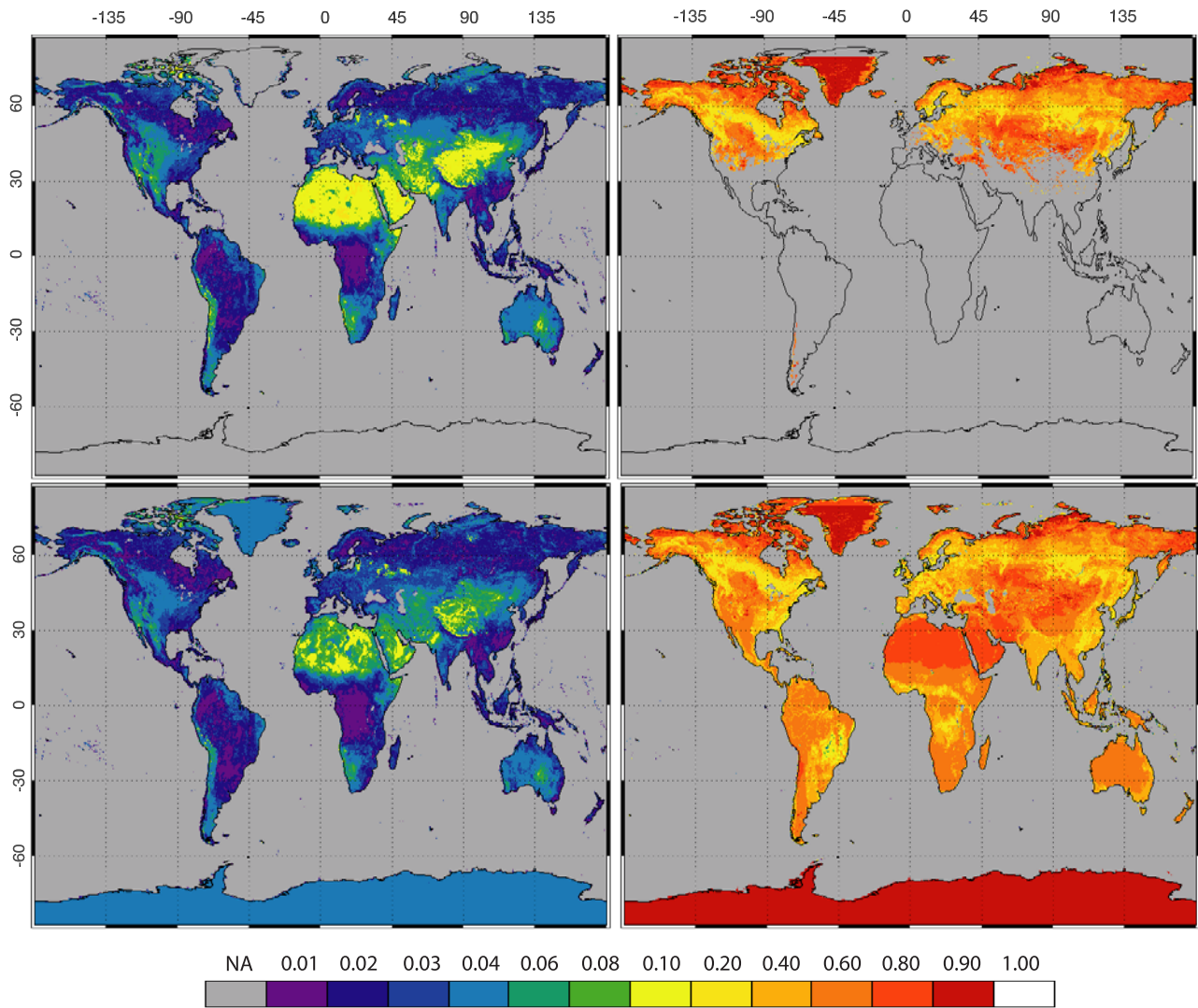
Figure 1. Albedo climatology for February derived from MODIS albedo data. (top) Before interpolation and wavelength correction. (bottom) After correction and interpolation. (left) Snow-free albedo. (right) Snow-covered albedo. For technical reasons the snow albedo values were also interpolated for desert regions.
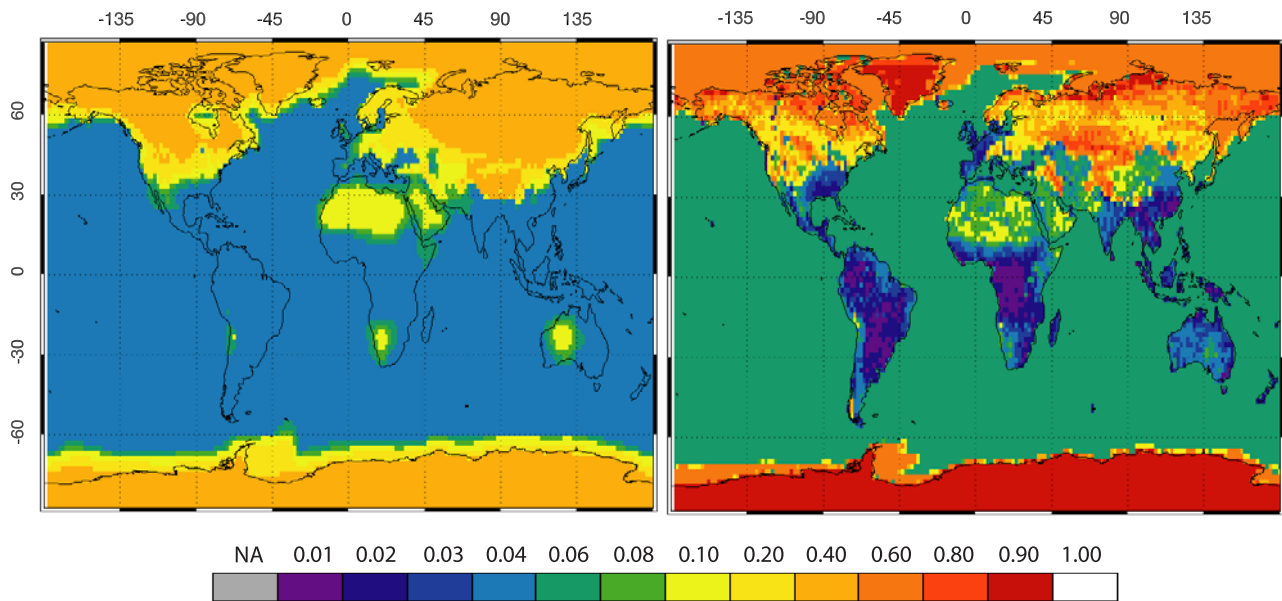
Figure 3. Monthly mean surface albedo map from the MOZART-2 model for February 2001 using the (left) old and (right) new albedo parameterization.
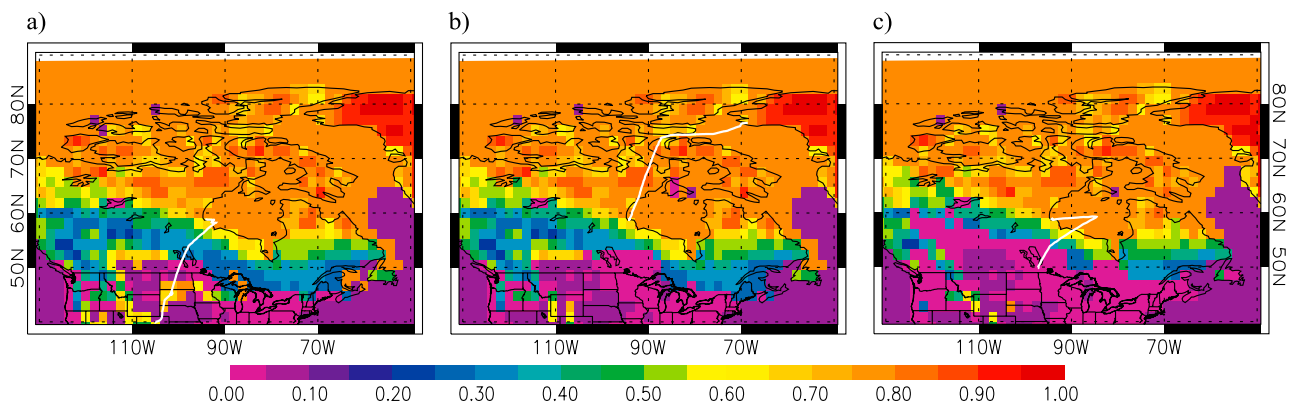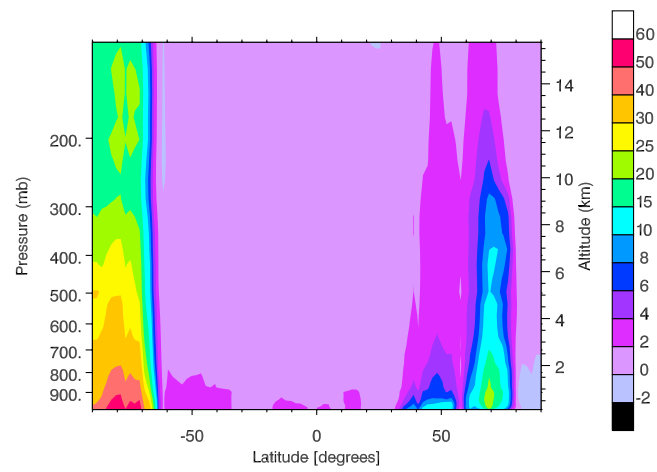

Figure 4. Albedo maps and flight tracks for (a) TOPSE flight 17 (8 March 2000), (b) flight 22 (24 March 2000), and (c) flight 32 (23 April 2000).
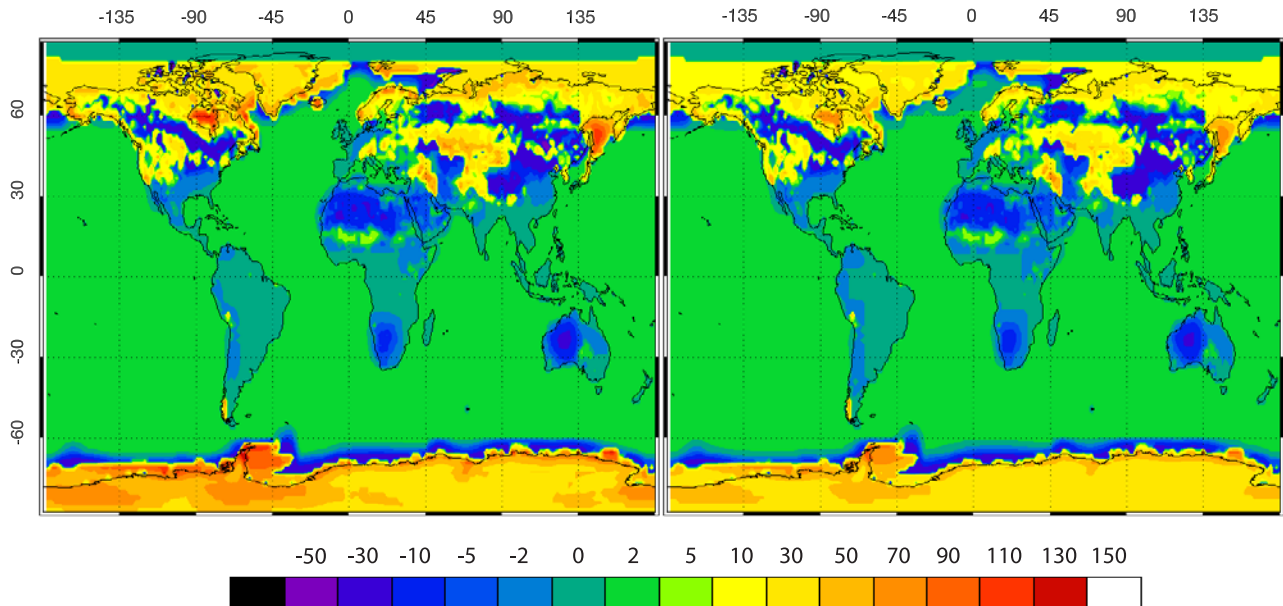
Figure 6. Relative changes (percent) of the February 2001 monthly mean value of the photolysis frequencies (left) $j(O_3 \rightarrow O(^1D) + O_2)$ and (right) $j(NO_2 \rightarrow NO + O)$.
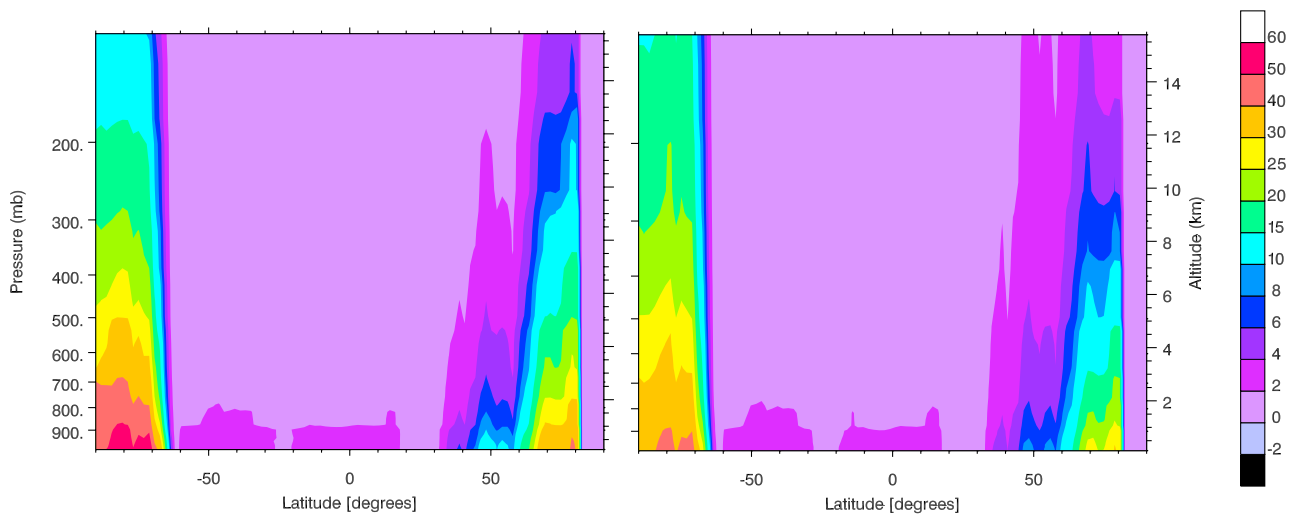
Figure 7. Zonal mean percent differences in monthly mean photolysis frequencies for February 2001: (left) $j(O_3 \rightarrow O(^1D) + O_2)$ and (right) $j(NO_2 \rightarrow NO + O)$.

Figure 9. Zonal mean percent differences of OH concentration for February 2001.